



Saranya, A, Kottursamy, Kottilingam, AlZubi, Ahmad Ali and Bashir, Ali Kashif
ORCID logoORCID: <https://orcid.org/0000-0001-7595-2522> (2022) Analyzing fibrous tissue pattern in fibrous dysplasia bone images using deep R-CNN networks for segmentation. *Soft Computing*, 26 (16). pp. 7519-7533. ISSN 1432-7643

Downloaded from: <https://e-space.mmu.ac.uk/630987/>

Version: Accepted Version

Publisher: Springer (part of Springer Nature)

DOI: <https://doi.org/10.1007/s00500-021-06519-1>

Please cite the published version

<https://e-space.mmu.ac.uk>

Analyzing fibrous tissue pattern in fibrous dysplasia bone images using deep R-CNN networks for segmentation

A. Saranya, Kottilingam Kottursamy, Ahmad Ali AlZubi, and Ali Kashif Bashir

Introduction

Researchers are focusing to provide economically low-price and accurate solutions for complex medical disease diagnoses. Transforming the image from the patient location to an expert location may arise errors. Removing unwanted information from the source image on both (patients and experts) sides is essential. Modern image processing is a deep learning-enabled filtering approach for removing the noises in the images. Fibrous Dysplasia (FD) is a genetic bone disorder it majorly affects children in their early bone development stage. If people failed to discover this kind of disease at an early stage, they have to pay for their lifelong with disabilities. The radiological images are taken from the local medical center and send that images to the experts.

There are many changes of getting the image to be corrupted due to the lighting, malfunctions in the sensing and surveillance devices, network errors, and receiver incompatibility devices. Removing these errors from the real-time images is a complex task. In this paper FD-affected person's images are referred from the National Institutes of Health (Fibrous dysplasia | Genetic and Rare Diseases Information Center (GARD) – an NCATS Program (nih.gov). xxxx), this repository has all genetic and generative disease information, clinical measures, and related publications.

Bone texture and shape feature extraction is a complex process that is solved by deep models with iterative training on the samples. Each level of training extracts the hidden details of an image, and it is further refined with the next level of training. The first layer extracts the features of pixel intensity variation, continuity among the edges, texture information, and shape modeling. The target image may consist of more than one object, the object dimension and shapes are trained with existing weights of many source images. It produces the shape learning information that is applied to the new image for segmentation and object detection.

Extracting and improving image information with different filtering is discussed in this paper. Many other related works are exploring the one way of image enhancement either on the pixel intensities or edge detections. The proposed combined approach comprises of the following techniques each used for unique purposes. Importing image surface defects by contour extraction, smoothing, and intensity corrections are covered with image blurring techniques. Shape edges and image fine details are noted with image sharpening techniques. Parallel edge processing is performed by Otsu segmentation that is helpful for larger and multiple objects in the images. Separating the uncertainty portion of the image by Region of Interest algorithms. Grouping a similar portion of the image by detecting the outliers with cluster-based segmentation. Extracting and Combining millions of features by RCNN algorithm to create the mask on the unusual portion of an image. Depending upon the need for image result transformation the researchers can select the techniques.

This paper discusses the bone image investigation techniques that support the discovery of the abnormal portion of an image. The proposed work of this paper is to combine the various image filtering techniques for concentrating the essential features of the image. The abnormal portion of the disease-affected samples is segmented with a masked RCNN algorithm. It helps to focus only on the affected portion instead of analyzing all other parts of the image. Applying different image filters

to the affected image at each level improves the classification accuracy. This combined approach helps to classify the image as an FD-affected or normal image.

Medical image noise removal and filtering approaches help to view the small changes in the affected area. Section [2](#) describes the techniques of bone properties with BMD values and imaging techniques. Section [3](#) discusses the different image processing techniques with 7 step building approaches of acquisition, segmentation, feature extraction, and classification. Section [4](#) discusses the algorithms of deep models for image segmentation and classification. Learning-based segmentation of mask-RCNN, FCN, and CNN architectures are explained with their advantages and limitations on feature processing. Deformable techniques of active contour, active shape models are also explained in this section. Section [5](#) discusses the results and experimental analysis of the conversed techniques on FD images.

Discovering bone mineral density

The relevant techniques of bone properties and abnormal conditions are addressed with the following algorithms. The literature covered with bone fracture detection, bone density and BMD analysis, imaging techniques, image filters and segmentation algorithms. Segmentation algorithm comprising set of divisions like image processing and deep learning.

Detecting the bone minerals in the target bone by Bone Mineral Density (BMD). Another important metrics is Bone Volume (BV) which is calculated by measuring the bone minerals per unit volume BV per unit volume. The BMD and BV are independent parameters that quantify the life span of the bone. Based on these values, the bone will be categorized into normal, osteopenia called low bone density, and osteoporosis called severe bone abnormality (Nazarian et al. [2008](#)). The bone image is the plot with the grid structure, each part is analyzed by computing the bone properties of density, surface quality, thickness, and bone structure model index.

The classification of normal and cancerous bones is modeled with Linear regression. Different types of tissue samples are tested to identify bone strength and stiffness.

$$Y = \beta_0 + x_1\beta_1 + x_2\beta_2 + \dots + x_n\beta_n$$

where β_0 is the bias, $\beta_1\beta_2\dots\beta_n$ are the coefficients, and $x_1, x_2\dots x_n$ are the input parameters.

In multivariate modeling on regression line with bone parameters of patients age, BMD values, gender, and ethnic are considered. The predicted BMD values for n patients are formulated here,

$$P_{bmd} = \beta_0 + \text{age}\beta_1 + \text{gender}\beta_2 + \text{ethnic}\beta_3$$

The bone deformity is happening with low bone minerals that reduce bone volume, thickness, and stress approximation ability. Various methods are computed to calculate the thresholds of bone minerals. BMD is a well-experienced technique for measuring the volume and thickness of the trabecular bone. BMD test results are based on the T-score and Z-score computed from the observed patient's scores with average scores. The average BMD scores are referred from the 30-year-old patients to categorize the density results. Mazees et al. proposed (Mazess et al. [1989](#)) a technique of Dual Energy X-ray Absorptiometry (DEXA) is the known technique for measuring the BMD/BV in the sample area (Gb/cm²) by considering bone region with soft tissues.

Two-compartment models are proposed to calculate the bone volume and BMD values from the computed tomography bone images of the affected region. The bone soft tissues are calculated with linear attenuation coefficients in the bone voxels. BV is computed using bone weight and percent volume in the region of sample pixels. Instead of segmenting the entire bone soft tissue region (Lin

et al. [2016](#)). Jing Zhang et al. proposed a model called the single energy scan model (Zhang et al. [2010](#)) for eliminating the beam hardening in the reconstruction of bone. Each input image considers the two submaterials of bone. Existing knowledge about the objects helps for segmentation and reconstruction. It extends the linear relationship between the voxels using the linear annotation coefficients. Separating the bone loss and structure from the bone is based on the bone mineral density by digital topological analysis (Wehrli et al. [2001](#)). This method classifies the bone regions into plates, rods, edges, junctions, and profiles from the trabecular bone representation. But its failure to classify the narrow and wide plates between the topological entities. The volumetric topological analysis method addresses the above problem by uniquely classifies its TB region. The perfect rods and plates of known etiology reduce bone loss. This method has been tested with the distal tibia and distal radius samples taken from the multidetector and micro-CT images (Saha et al. [2010](#)).

Rao proposes (Rao et al. [2011](#)) the techniques for detecting dengue fever with real-time data sets using wrapper feature selection. The most fitted features are identified by the genetic algorithm and decision tree-based prediction is performed with generated rules. Tweetlueza (Alkouz [2019](#)) is a model created for categorizing influenza-related conversion and hospital appointments from tweets. Processing these diseases-related information is used to predict the disease trends. The health data from the critical patients with monitoring devices like sensors, ECG signals, temperature measuring kit, and infection investigator are collected. Then transform this sensitive information to medical advisors for taking immediate action. Internet of Things (IoT) enabled devices are collecting chronic disease data from the patients and send the updated status report to the monitoring agent. Disease surveillance (Alabdulatif et al. [2019](#); Koutkias et al. [2005](#); Ram et al. [2015](#); Buckeridge et al. [2012](#)) with the constructed framework enables quick updating of the complex situations and analyzing the disease-affected trends. Many pattern analyses can be performed with this real-time data handling. IoT devices are attached to the person for informing and count updating the COVID affected cases. This system will notify to maintain a 2 m distance from the other persons. Also check the oxygen level, risk ratio, body temperature, and cough (Vedaei et al. [2020](#)).

The classification system is proposed for classifying the fractured portion from the normal bone image. The fracture regions are comparatively smaller than normal regions. The suspected regions are divided into volumes of interest. From all these regions, 29 parameters are extracted as features. These features are considered for classification algorithms to classify fractured and non-fractured (Korfiatis et al. [2017](#)) regions. To identify Biomarking in fracture zone is done with the sequential forward floating selection technique. TB thickness with bone marrow tissue interconnected spacing is measured by the star line tracing method. This method is based on voxel size comparison. This method also eliminates the digitization association with other conventional algorithms (Liu et al. [2014](#)).

Daniela Giordano et al. proposed a new segmentation technique for finger, wrist bones as epiphysis/metaphysis region of interest (EMROI) and carpal region of interest (EMROI). These algorithms are tested with below 10 years males and below 7 years of female patients. Extracting bone from the soft tissue is trained with anatomical knowledge of the shape models, and the major drawbacks of the wrist bones feature extraction are solved by curvature function (Giordano et al. [2010](#)). The additional models are also developed to enhance the shape identification along with EMROI. Another approach of TB thickness estimation is computed by the structure-based algorithm (Ang et al. [2019](#)), which separates the cortical from the TB using binary images. The cortex thickness value is assigned as a threshold to separate the cortex from the bone. This method has been tested

with multiple datasets of micro- μ CT images, multidetector CT images, and high-resolution-based peripheral quantitative CT image (HR-pQCT).

The partial segmentation methods naturally incorporate the edge detection mechanisms to detect the bone region with region-boxes (Ohlsson et al. [2017](#)). The trabecular and cortical bone were tested with Gaussian and threshold-based filters. These kinds of segmentations are suitable for spine and hip fractured patients. The HR-pQCT is a low radiated technique that measures bone deformity with the density and microstructure analysis of bone (Jong et al. [2016](#); Areeckal and Kocher [2018](#)). Quantitative UltraSound (QUS) is the best cost-effective mechanism in terms of less radiation. It applies the sound waves of 500 kilo Hz to 1.25 mega Hz on the affected bone region to measures the reflections (Hans and Krieg [2008](#)). Broad-Ultrasound Attenuation (BUA) and Speed of Sound (SOS) are the major bone tests for plotting the refraction range. These techniques are extended to calculate the high-risk fractures with stiffness index, QUS index, amplitude index, and combined scatter (Diez-Perez et al. [2007](#)). The limitation of calcaneal QUS is solved with a measure of the device-specific threshold. In the case of temperature, variation is identified; the QUS is not good for measuring hip and spine fractures (Hans et al. [2003](#); Njeh et al. [2000](#)).

Framework for bone image analysis

Image pre-processing techniques are widely used to discover bone deformities with different types of imaging. Any bone image of the affected area is undergone with image processing techniques to reconstruct the old images into a detailed image for investigation. In the quantitative imaging ("The use of biomarkers in clinical osteoporosis." [2016](#); Looker et al. [2000](#)), biochemical markers are used to measure the bone minerals of osteocalcin, C-terminal collagen telopeptide, urinary hydroxyproline, collagen crosslinks, bone-specific alkaline phosphatase, etc. These results can address the results of bone formation and deformation risk ratios. Generally, image processing techniques (Gonzalez and Woods [2002](#)) are formed the 7-step building approach. The initial step called image acquisition has been done with many dedicated and accurate imaging modalities. Fibrous dysplasia images are taken to examine the details of anomaly portions in the image. Also discover the type of abnormality using the image processing techniques. The second step is image enhancement that is used to transport hidden detail and highlight essential features of the image; the third step combines image restoration and color image processing. That improves the appearance of an image with color modeling in digital aspects.

The fourth step is image compression; it reduces the spatial information between the pixels to provide the exact storage space to save and transform the image. Steps 2, 3, and 4 are generally called image pre-processing techniques (Ribeiro [2014](#)). The fifth step is image segmentation; many algorithms are available for segmenting the image into small regions with its constituent parts. Step 6 is extracting the essential features of the image and its detail and description. This can be done in two ways manual (machine learning) or automated (deep learning). The final step is objected recognition and classification (Areeckal and Kocher [2018](#)).

Image acquisition

Image acquisition considers correcting the image dimensionality and resolution for processing the tasks, when the high dynamic range of input images is generated from the source. It is not suitable for visualization of conventional display devices because of variation in luminance level. For reducing these kinds of issues, Gabriele et al., (Guarnieri et al. [2010](#)) proposed the algorithm called Retinex theory of vision to reduce the high dynamic range without affecting the image visual sensation. The

resolution limitation of an image is solved by pixel super-resolution. It combines the information of various low-resolution images (O'Reilly et al. [2013](#); Reeth et al. [2012](#); Kennedy et al. [2006](#)).

Image segmentation

Segmentation is used to diagnose anomalies in the region of the image. Many improvisations have been taken to automate the segmentation algorithm, because manual segmentation texture analysis takes more time and it provides the intra-observer and inter-observer variability. An automated segmentation algorithm reduces the noise, subjective error, and variations in acquisition conditions. Analyzing the bone texture in consecutive ROIs is used to diagnose a bone disease of fibrous dysplasia. Automated segmentation algorithms provide fast and accurate results by combining the filter back projections and anatomical knowledge. Menske et al. proposed (Manzke et al. [2009](#)) the technique that reconstructs the image portion into an anatomy shape model using intra-surface generation. Extracting the features from the target image helps to identify the pattern of all other similar images. The common salient features of an image are color, texture, luminance, and depth. These features are extracted from 2 and 3D images by the discrete cosine transform (DCT) (Manzke et al. [2014](#); Fang et al. [2012](#)). DCT coefficients are efficient in extracting the salient features from the high energetic sources.

Classical image filters for edge detection

Some of the classical filters and edge detection algorithms are discussed here for reconstructing the images with reduced noise. Edge detection is used to detect the meaningful discontinuity gray color intensity values in the images. Initial and next-order derivatives are used to detect the discontinuities; generally, first-order derivatives take the gradient for processing the image. The gradient function of $f(x, y)$ is defined as,

$$\nabla f = \begin{bmatrix} g_x \\ g_y \end{bmatrix} = \begin{bmatrix} \partial f / \partial x \\ \partial f / \partial y \end{bmatrix}$$

The magnitude conversion of vector $f(x, y)$ is,

$$|\nabla f| = \sqrt{g_x^2 + g_y^2} = \sqrt{(\partial f / \partial x)^2 + (\partial f / \partial y)^2}$$

The second-order derivative is computed using the Laplacian method,

$$\nabla^2 f_{x,y} = \partial^2 f_{x,y} / \partial x^2 + \partial^2 f_{x,y} / \partial y^2.$$

An important consideration in the first and second derivatives for edge detection is where the initial derivative of intensity, value is larger than the specific threshold, and the subsequent derivative of the intensity is almost zero.

Sobel Edge detection is detecting the image edges in horizontal, vertical operations and the coefficients about derivatives are not permanent; they can be used to the researcher's requirements.

$$|\nabla f| = \sqrt{g_x^2 + g_y^2}$$

Prewitt edge detector parameters are the same as the Sobel filter, but it is computationally simple than other methods. The limitation of the Prewitt method is it produces noise results. The next method is Roberts edge detection which is the earlier edge detectors in the image analyzing technique. It uses to approximate the difference of the derivatives with adjacent pixels. It is not an asymmetric but very fast algorithm and not suitable to detect the edges with multiple of 45 degrees. Laplacian of Gaussian detector (LoG) uses the Gaussian function,

$$G_{x,y} = e^{-x^2+y^2/2\sigma^2}$$

where σ is the variance; it determines the cost of blurring. LoG gives the two effects; it reduces the noise from (smooth) the image and calculates the Laplacian that provides the double edges. The zero-crossing detector is the same as the Laplacian algorithm and the difference is convolution. That is carried out with a particular filter function. The most powerful edge detection algorithm in a functional edge model is a Canny edge detector. It uses Gaussian filters for smoothing of specified deviation (σ) to reduce the noise and finding the local maximum gradient for edge detection. It follows the threshold method to differentiate the ridge pixels with values greater than t_2 said to be strong (t_1 , t_2 are two threshold values). The values lying between t_2 from t_1 are said to be weak pixels. Segmenting (Santhoshini et al. [2013](#); Ghosh et al. [2011](#)) the bone images using these algorithms helps to identify the abnormal region from the entire image.

Deep networks for medical image processing

Deep networks are efficient in detecting and recognizing abnormalities in medical images. An automatic and quick segmentation helps to diagnose and locate the tumor, fracture, blood leakages in the vessels, cardiac blocks, and brain encephalitis. Various tasks are involved in extracting useful information from the medical images. It has been divided into image segmentation, object recognition, object localization, and classification. Segmentation is broadly classified into semantic segmentation and instance-based segmentation. Semantic segmentation trains and learns the features to detect the objects in the frame, whereas instance-based segmentation detects the objects and describes them with different colors for efficient recognition and classification. Particularly CNN has higher consideration on medical image analytics, because of their multiple levels of abstraction. Each level of the CNN network consists of multiple layers. Every layer has inbuilt neurons and added weights. Extracting the features from the image is an effective process that decides the correctness of the predicted result. The Fully Connected CNN (FCN) takes the input as an entire image and produces the result as dense segmentation. Processing with the entire image increases the spatial resolution loss because of its max-pooling layers in each stage (Long et al. [2015](#); Ren et al. [2016](#); LeCun et al. [2015](#)), feature extraction and segmentation.

To overcome this issue, upsampling is performed with activation to reduce the loss of spatial resolution. U-net is one type of CNN architecture that is extremely outperforming the medical image U-net having skip-connection modules that help to recover the entire spatial resolution of an image with multi-level feature fusion. These functionalities are important for processing image segmentation and classification. Yin et al. proposed the guided filter preserves the edge information and restores the spatial information loss from the thin-layered images.

The guided filter reduces the noisy effect by downsampling the feature operations (Yin et al. [2020](#)). Figure [1](#) depicts the framework of image segmentation to class label prediction. Without affecting the segmentation accuracy impact of 2D image convolutional modeling into the 3D image is a challenging task. That has been addressed by increasing the number of convolutional layers to 15 ("Automatic [3D](#) bi-ventricular segmentation of cardiac images by a shape-refined multi-task deep learning approach." [2019](#)). Using the anatomical shape information gives the knowledge about the human parts, which helps to segment the image effectively. In many cases, the scanned images have chances to affect by irreducible noise and damages in the image portion. In such cases, these kinds of anatomical prior knowledge about the human organ shape models support training and detect the correct portion of human parts. Atlas propagation-based shape modeling is used to train the prior knowledge of an image; it reduces the spatial information without affecting the shape model. It does not require the Region of Interest (ROI) segmentation. Anatomical knowledge supports

reducing the loss in motion object on cardiac MR segmentation (Oksuz et al. [2019](#)). The MR high-quality images are corrected with the k-space loss function to detect the objects and correct the objects based on prior information; then the image reconstruction network produces the segmented images. Training the CNN with shape prior information is a challenging task; it has been overcome by a generic training strategy with global shape information (Cook "Anatomically constrained neural networks (ACNNs): application to cardiac image enhancement and segmentation.",, et al. [2017](#)).

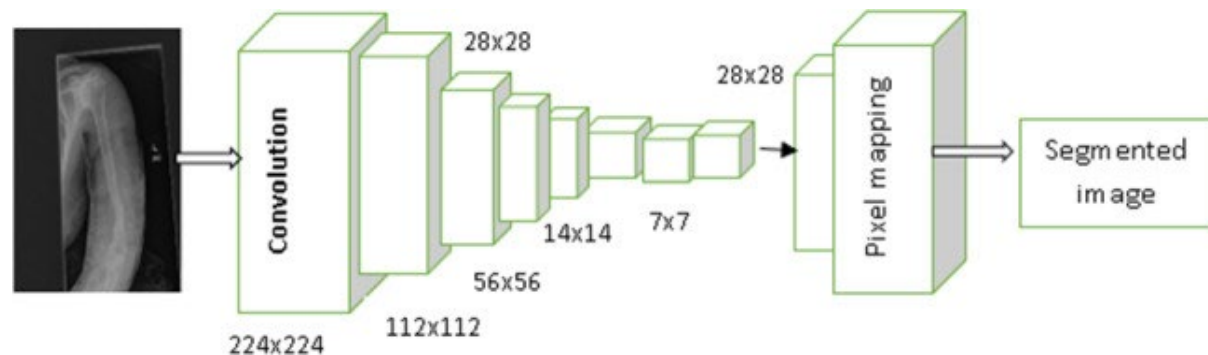


Fig. 1

Deep models for image segmentation

Brosch et al. introduce the shortcut connections of convolutional layers that integrate the high- and low-level features (Brosch et al. [2016](#)). This network consists of two pathways, convolutional pathways learn and extract the abstract and high-level features, whereas the deconvolutional pathways predict the segmentation. This joint approach of optimization allows automatic feature learning at different scales of input. The user interaction-based image segmentation helps to identify the wrong segmentation using the back propagatable Conditional Random Field (CRF) (Wang et al. [2018](#); Zhao and Xie [2013](#)).

The new method of polyp segmentation does not ensure the information of multi-level contextual and extracts the features of different fields of view with multiple scales of an image using continuous multiple decoder and encoder network (CDEC). The boundary-emphasized data augmentation technique is proposed for learning the background and foreground regions with dice loss function (Nguyen and Lee [2019](#)). The multi-level features extraction and individual level feature refinements support the discovery of the automatic defined solution of prostate image segmentation in the high dimensional images (Wang et al. [2019](#)). An automatic hierarchical cascade of CT image information is used for classifying the image into different segments depending on the superpixel resolutions (Farag et al. [2016](#)). The random forest and deep neural network models are compared with the boundary-preserving superpixels. Many deep learning-based segmentations models are discussed in Table [Table11](#) with their advantages, limitations, and applications (Minaee et al. [2021](#)).

Table 1

Different segmentation algorithms for medical image processing

Algorithm	Description	Advantages	Limitations	Applications
Region of interest (ROI) segmentation (Sun et al. 2019)	This separates the object into multiple regions or sub-tasks	It performs well for contrast objects. The cost of computation is less and operating speed is high	grayscale pixel overlapping between the object and background	Cardiac image segmentation, fracture detection, tumor detection
Edge detection segmentation (Kwok and Constantinides 1997)	Detects the boundary based on the discontinuous local features	It is suitable when the objects are differentiated by contrast	Not suitable for detecting multiple edges	Posture detection
Segmentation based on clustering (Huang et al. 2019)	It separates the images into homogeneous clusters	It performs well for small datasets	Computation time for clustering is high. It does not detect the non-convex clusters	Skin diseases, blood infections
R-CNN (He et al. 2017)	It gives the object mask, bounding boxes, and class labels	This approach is flexible for small and large datasets. It is an efficient technique and simple computation	Training time highly depends on the details of an image	Instance-based segmentation
Fully convolutional layers (Long et al. 2015 ; Seyedhosseini and Tasdizen 2015)	It combines the semantic and appearance information	It produces detailed and accurate segmentation	Downsampling reduces the resolution of an image with large factors	Brain tumor, iris, and skin lesion segmentation
Convolutional with graphical models ("Conditional random fields as recurrent neural networks." 2015)	The final layer of CNN is combined with CRF	Able to predict the localization of segmentation boundary	Difficult to reduce the spatial information	Natural language processing, social network analysis

Algorithm	Description	Advantages	Limitations	Applications
Encoder-decoder based models (Ronneberger et al. 2015 ; Milletari et al. 2016)	U-net CNN is used for medical image segmentation with segmentation	It requires fewer training samples and initiates global localization and context extraction	Slow down the learning process in the middle layer	Micro-biopsy image segmentation
	V- net based on dice coefficient for the whole volume of image segmentation	Used to provide seamless segmentation in volumetric data	Poor pixel correlation between foreground and background images	Lesion segmentation
Multi-scale and pyramid network-based models (Lin et al. 2017)	Merging the low- high level features to form the feature pyramid	It reuses the multi-scale features maps between different layer	It does not detect the small objects	Salient object segmentation
Recurrent neural network (Byeon et al. 2015)	Performs pixel-level segmentation with long short-term memory	Efficient texture and spatial parameters learning	slow process due to its sequential nature	Motion object segmentation
Dilated convolutional models (Chen et al. 2017)	Additional parameters of dilated rate are added to CNN	It overcomes the decreasing resolution and improved boundary for object localization	Poor segmentation when the image consists of multiple slices	Real-time segmentation

Ren et al. proposed the CNN with a regression model to assess the bone age using the fine attention maps between the segmented images. It detects the outlier portion of the image to effectively with dynamic attention loss models ("Regression convolutional neural network for automated pediatric bone age assessment from hand radiograph." [2018](#)). Removing the haziness in the images by computing the superpixel intensity values among all regions. Comparing each pixel intensities individually with extreme intensity superpixel values. Reducing the atmospheric light discontinuity is identified with a transmission map and a guidance filter is used to highlight the textures, edges, and smoothing information in the image ("Real-time image dehazing by superpixels segmentation and guidance filter." xxxx). Highlight the pixels by reducing the intraclass variance effect in the

hyperspectral images. Optimizing these kinds of spectral parameters improves the maximum likelihood of pixel similarity with reduced spatial dimensionality (Ahmad et al. [2017](#)).

Image quality can be destroyed and chances of malfunctioning in medical records are quite common nowadays. Breast cancer images are received from experts in highly infrastructure hospitals. Through deep networks transfer learning cancer diagnostic models are proposed. It has adopted in the edge server for another doctor's clarification. This method will be useful for rural hospitals those are not having high infrastructures (Yu et al. June [2021](#)). Transfer learning helps to improve the diagnostic accuracy over other methods. Ensuring the privacy of medical records and patient's health information needs more attention in the electronic transfer mechanism. The COVID-19 patients records are necessary for tracking and verifying the health condition in future aspects. Blockchain (Tan et al. [2021](#)), ElGamal Blind Signature (Sun et al. [2021](#)) embedded security mechanisms are used for keeping these health records safe. Also, it uses to reduce the data storage and overhead of single-point failure. Securing the health records IoT edge devices using access policy expression. It encodes the data with online and offline encryption method and outsourced decryption method (Li et al. [2021](#)).

Image classification based on abnormality

Capsnet architecture (Saif et al. [2019](#)) is used to detecting and classifying musculoskeletal bone disorders by overcoming the drawbacks of CNN. Increasing the input image dimension helps to view the details of an image and the local feature detector is enabled with convolutional layers. It predicts the intensities of active pixels in the encoder part. Then the decoder capsule consists of optimized capsule class labels to predict the abnormalities, even the image as lighting and orientation issues.

This reduces the interference of max pooling. For detecting the abnormality in the spine curves using Adaptive Error Correction Net (AEC-Net), it is proposed by Chen. It calculates the cob angels and landmarks of the spine curve and a high precision loss function is applied to correct the error with an approximation based on deep learning approaches (Chen et al. [2019](#)).

Inception ResNet-v2 (Kwon [2020](#)) is used to extract the Knee osteoarthritis features from the gait and x-ray images. Then the Support Vector Machine (SVM) is used to classify the multi-class abnormality prediction. Classifying the other diseases using deep networks with medial images creates a major impact on learning-based disease prediction. Initially, the CNN is trained with ImageNet features then the transfer learning is applied to detect the cervical cell dataset abnormalities with score (Zhang et al. [2017a](#)). Analyzing the microscopic images with different deep network architectures gives opportunistic learning on the disease pattern (Xing et al. [2017](#)). The tested deep models are CNN (Cireşan et al. [2013](#)), rotational invariance is improved with arbitrary object rotation and mirroring techniques, RNN (Zhang et al. [2017b](#)) processes the sequential data of gene expression and protein sequences, FCN ("Deeply-supervised nets." [2015](#)) performs the end to end convolutional net in a deeper connection, and stacked autoencoders (AE) (Su [2015](#); Mallick et al. [2019](#)) are used to reduce the reconstruction error on the with the noisy gradient map on the original image and deep belief networks. Image compression with feature reduction properties enabled in deep wavelet autoencoder that shrinks the image feature set and the classification of brain tumors and blood leakages with deep neural networks. Extracting the features (Kumar et al. [2016](#)) from the image datasets using different types of CNN architectures and the ensemble techniques are applied to predict the abnormality class labels.

The RCNN algorithm is the expert option for predicting and segmenting the abnormal portion in an affected sample. Initially, model weights are defined for training and prediction. Perform an active

selective search to extract multiple regions on the input image. These extracted regions are of different scales and sizes. Each proposed region is labeled with a bounding box. Based on the network requirements, every region is resized. The extracted features and respective labels are taken as an example; it is used to classify an object.

Results and discussion

BMD values of spine bone (Bachrach et al. [1999](#)) include the attributes of patients id, age, sex, ethnic and BMD values of 1003 patients. Linear Regression (LR) model is adopted to express the relationship between the observed input attributes on target BMD. The multiple linear regression model is expressed as,

$$\text{Spine_bmd} = -0.0001 * \text{pid} + 0.0244 * \text{ethnic} + 0.0252 * \text{age} + 0.0798 * \text{gender} + 0.4593.$$

The observed parametric results and error values are correlation coefficient (r) 0.6549, mean absolute error (MAE) is 0.1119, root-mean-squared error (RMSE) is 0.1389, relative absolute error (RAE) is 74.164%, and root relative squared error (RRSE) is 75.4808%. Figure 2 depicts the combination of different input features with the predicted BMD values. Each iteration generates different intercept (β) and coefficient values based on the influence of feature attributes with the target attribute (spinebmd).

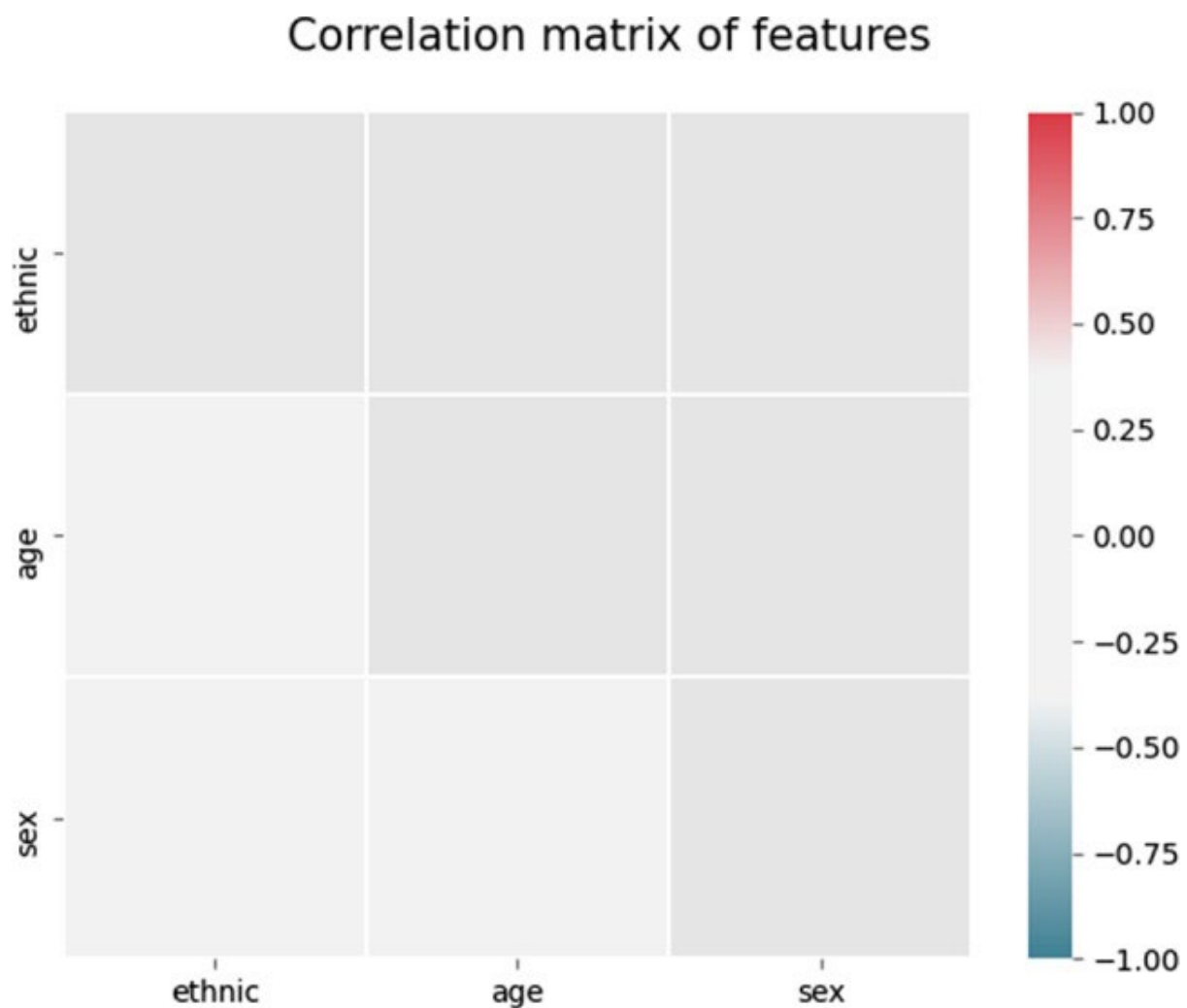


Fig. 2

Confusion matrix of feature variants

The distribution of predicted BMD values with the patient's age is shown in Fig. 3 with regression 0.37. The residual error is calculated with the observed and predicted results. The error values are interpreted with a zero-intersection regression line shown in Fig. 4.

$$\mu; \text{Log-likelihood} = L(\mu, \sigma^2; x_1, \dots, x_n) = -n/2 \ln 2\pi - n/2 \ln \sigma^2 - 1/2\sigma^2 \sum_{j=1}^n (x_j - \mu)^2$$

where μ is denoted as mean, σ is standard deviation and (x_1, \dots, x_n) testing samples. Depending on the attributes of age, sex, and BMD values, the two clusters are assigned by density-based cluster algorithm. Cluster 0 considers the prior probability of 0.4547 with age (mean = 16.1893, StdDev = 4.2559), 456 male patients, and spine_bmd (Mean = 0.8981 StdDev = 0.1881). Therefore cluster 1 considers the age (Mean = 16.4272 StdDev = 4.427), 547 female patients, and spine_bmd (Mean = 0.989 StdDev = 0.1696). The estimated log likelihood is -3.26923 calculated with above equation.

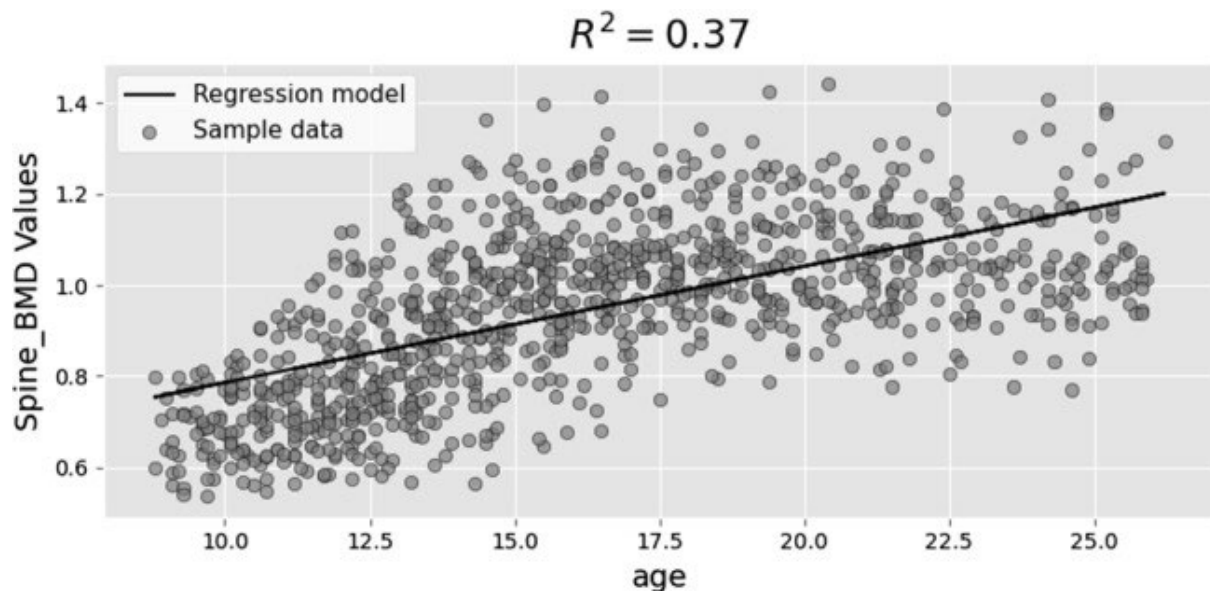


Fig. 3

Spine BMD value prediction

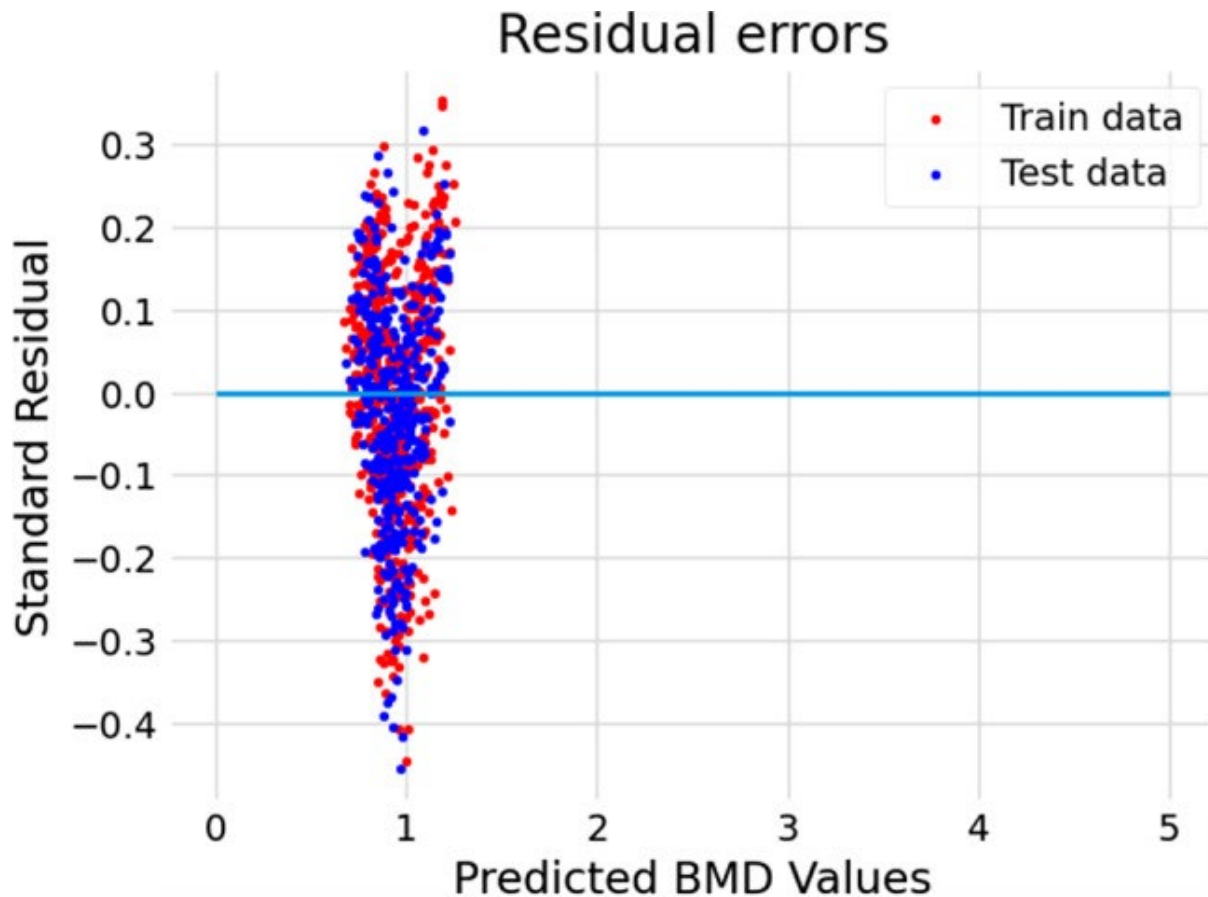


Fig. 4

Variational score of predicted results

Image enhancement techniques are used to screen the noisy information from the target image with ground truth values. Learning enabled filtering and image denoising forward the processed image to the object (tumor/ lesion) recognition. This part discusses the experimental investigation of various pre-processing and image segmentation techniques. Image is represented as discrete from continuous pixel representation.

$$f \rightarrow f_a, b = m_a, b \times n_a, b$$

where f is the image function; it is described as a discrete closed set of pixels $m \times n$ and the position of the pixel is (a, b) . In terms of intensity correlation with pixel positions is denoted as,

$$f \rightarrow I = f_a, b, a, b$$

When the image filtering is applied in the original image, the Nearest Neighboring (NN) values are averaged,

$$NN_t = f_a, b = x_a + y_b + z_{ab} + w$$

$$NN_{4p} \rightarrow a+1, b, a-1, b, a, b+1, a, b-1$$

The above form is used to calculate the 4 neighboring pixels on the position at a, b .

$$NN_t'p = f_a, b = \sum_{i=1}^t \sum_{j=1}^t x_{ija} y_{bj}$$

$$NNt^{-}p=\prod t=t',t''NNtpUNNDp$$

where t', t^{-} are considered the higher range of pixel distance coverage. The noisy image is represented as in a known way,

$$f'a,b=fa,b+\eta a,b$$

$$\text{Average filter}, f'a,b=1mn\sum_{x,y\in Sab}fa,b$$

$$\text{Median filter}, f'a,b=\text{median}_{mnx,yx,y\in Sab}fa,b$$

Median filters are not damaging the object edges; it pertains the original value of an image without affecting its adjacent values, whereas a Gaussian filter is used for smoothing the images and reduce the noise by blurring the image. The repeated average filter replaces the traditional Gaussian filter drawbacks by giving more attention to the edges (Hassan et al. [2019](#), [2021](#)). Combining the segmented superpixels to construct the blur map and defocus them with transductive mapping.

$$\text{Gasian filter}, f'a,b=12\pi\sigma^2e^{-a^2+b^2/2\sigma^2}fa,b$$

$$\text{Convoltion filter } f*ga,b=\sum_{y=b-hb+h}\sum_{x=a-wa+wf}x,ygx-a,y-b$$

Convolution filter is a spatial filter and the kernel $g(a, b)$ can be adjusted with effective width and height. Applying multiple image acquisition and enhancement techniques gives the details of an image. Figure 5 shows the different types of filters on fibrous dysplasia affected sample image. These kinds of pre-processing approaches are used for extracting the feature of Grayscale pixel intensity, texture, and smoothing values. This step gives an efficient way of locating and segment the object from the image. Six types of segmentation techniques are available in medical image processing. There are 40,561 images tested with these filtering and segmentation algorithms. K-Cross fold validation is used to separate and iterate the data items. All the sets of inputs are tested and evaluated with K bundles. Input images are split into two groups as training and testing with a 70:30 ratio.

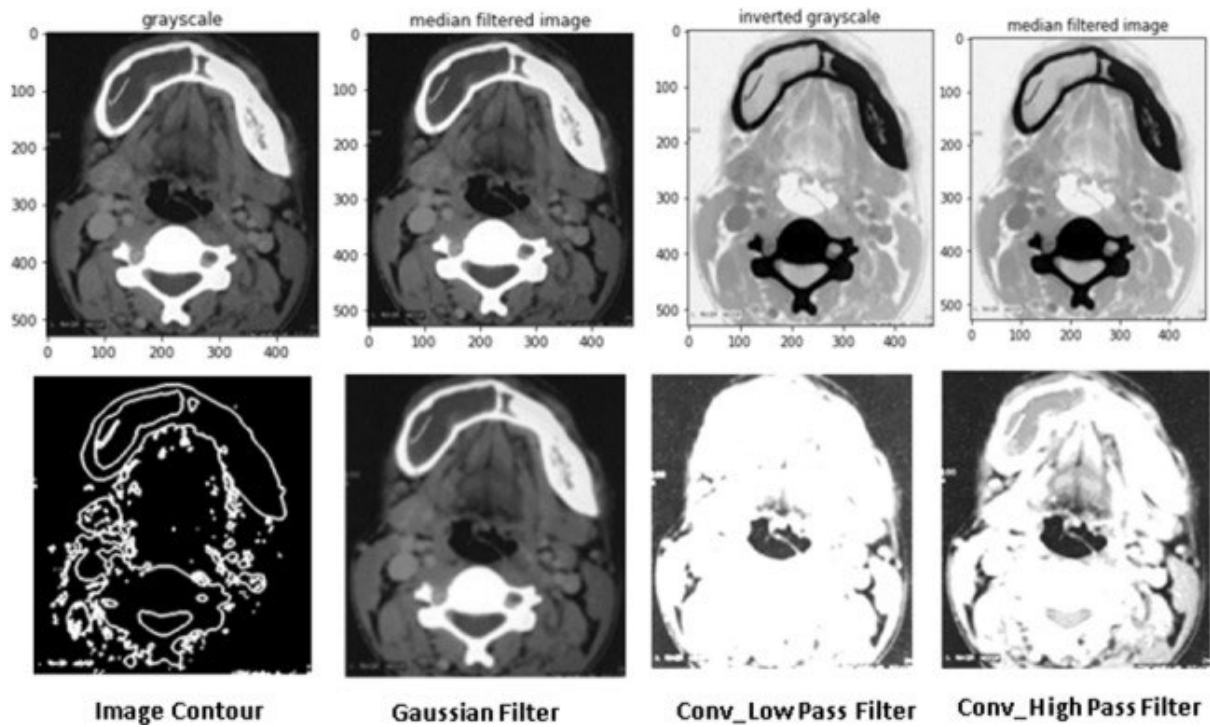


Fig. 5

Different filters on skull dysplasia images

An input image is separated into a set of pixels of (i,j) , and it compares the pixel intensity values of any position (a,b) to the specified threshold intensity value (T) . Depending on the threshold value, the image pixels are grouped and used for object identification. This algorithm is efficient for an object that has high or low intensity than a background image. It does not suitable for multi-peak intensity valued images, and it works for low noisy images. The threshold value may be constant or variable depending on the researcher's consideration.

Binary segmentation $S_{bin} = \{i,j < T, \text{for } i,j \rightarrow 0; i,j > T, \text{for } i,j \rightarrow 1\}$.

Otsu Segmentation is automatically discovering the constant threshold value based on the intensity distribution. It supports the bimodal images that have two different pixel variations. It can be represented as, p and q , which are two peaks of intensity distribution,

$S_{otsu} = p \mid q \rightarrow T_{\text{constant}}$

$p = \sum I = 0 \text{ to } t \text{ f}(I_i, j) \rightarrow c_0, q = \sum I = t+1 \text{ to } n \text{ f}(I_i, j) \rightarrow c_1$

where c_0, c_1 are pixel distributions and t represents as pixel variation limit.

Edge-Based Segmentation considers the features of object edges that have high relevant information. Edges add meaning to the objects, whereas edge detections reduce image size by eliminating the less relevant information (noise).

It detects the edge values based on the pixel density, gray level discontinuities, texture, color, contrast, and brightness, etc.; edge segmentation algorithms are divided into gradient level and grey level. Figure 6 shows the local and global threshold-based segmentation of FD images and different types of edge detection techniques applied to the image. OpenCV color detection methods are used

for detecting abnormal portions of the RGB color images (Mehra et al. [2020](#)). The background image color has differed from the target portion of the image.

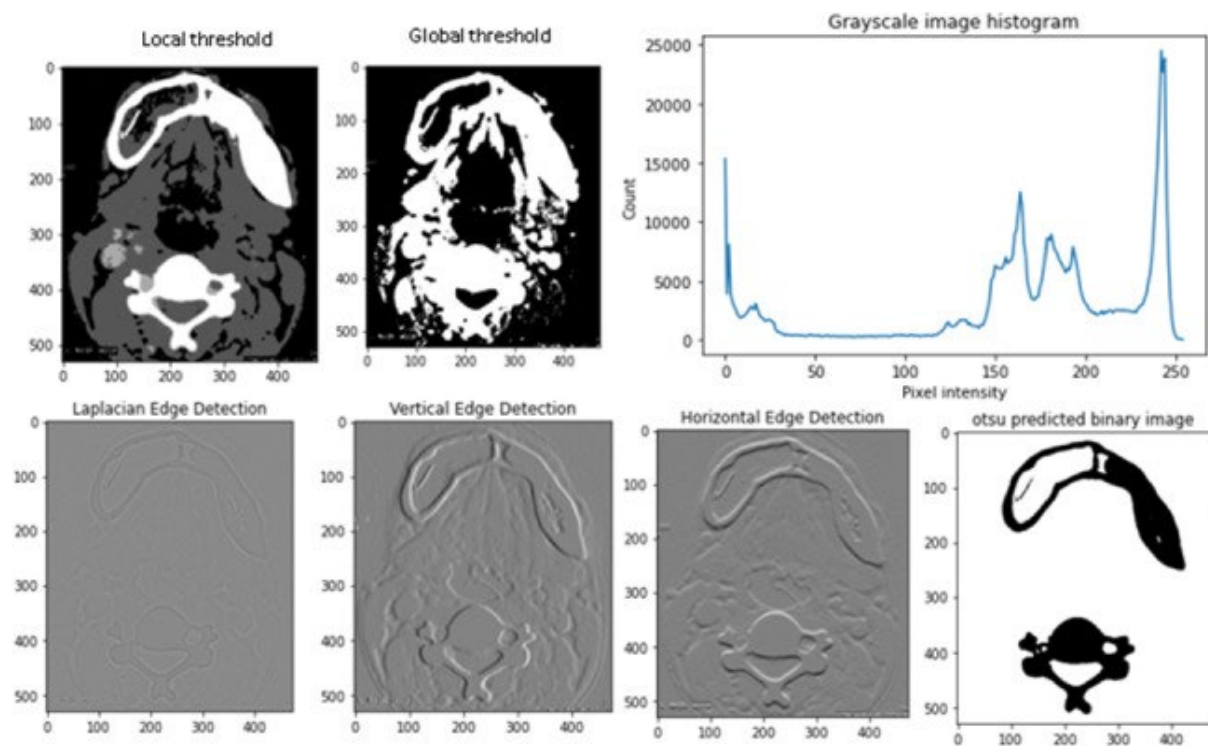


Fig. 6

Threshold segmentation and edge segmentation

Region-based segmentation has split the region as small and larger based on the similarity. The seed value is selected among the pixels; it may be random or pre-defined constraints. The seed value is compared with other pixels either to merge the regions or shrink the region. Region-based segmentation of FD wrist bone and craniofacial bones is shown in Fig. [7](#).

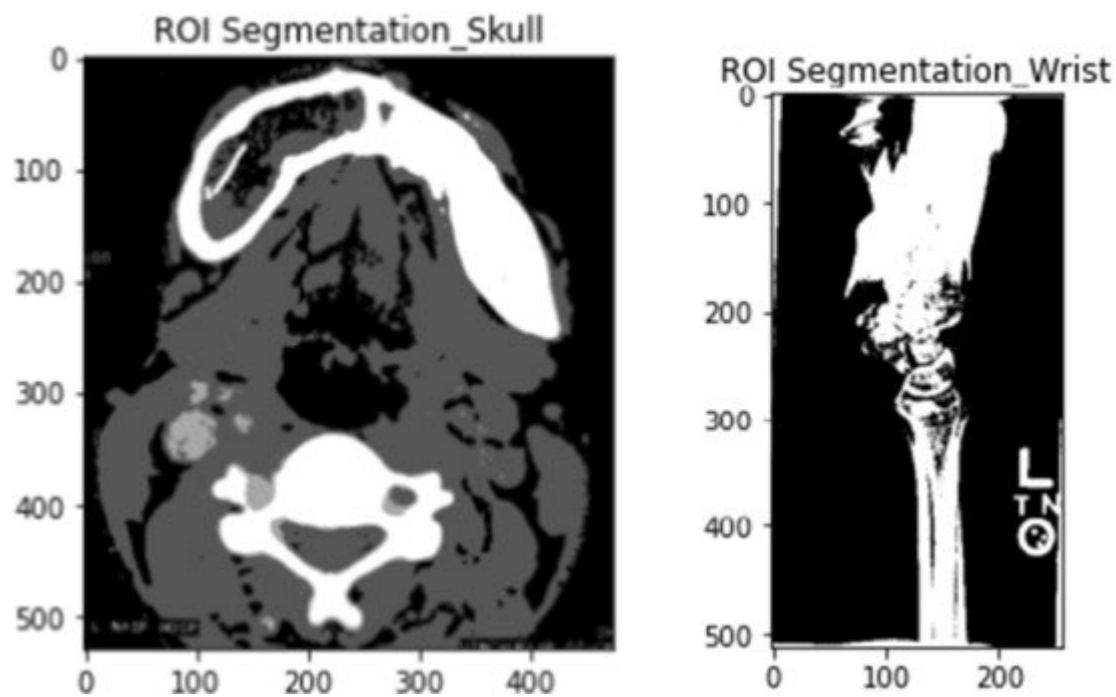


Fig. 7

Region of interest segmentation

The Watershed segmentation algorithm is an efficient and easy method for segmenting images with region processing. The initial kernel points are selected manually or non-manually inside the region, which grows around similar seed points among the regions. It works on the hybrid method; the image surfaces are considered as topographic and water is flooding to fill up the minimum catchment basins to extract the boundary of the ROI (Meyer [1994](#)). The disadvantage of this algorithm is over-segmentation due to random noise in the image; improvisation in the watershed algorithm is placing the markers to discover the local minima to eliminate the noises. This marker-controlled watershed algorithm is used for segmentation and measures the metacarpal bone using cortical radiogrammetry (Areeckal et al. [2018](#)), and also wavelet decomposed images are used to perform segmentation on trabecular bones presented in micro-CT images (Fourati and Bouhlel [2011](#)).

It achieves lower segmentation errors comparing to all other algorithms. Figure [8](#) shows the watershed image segmentation with dilation and distance transformation.

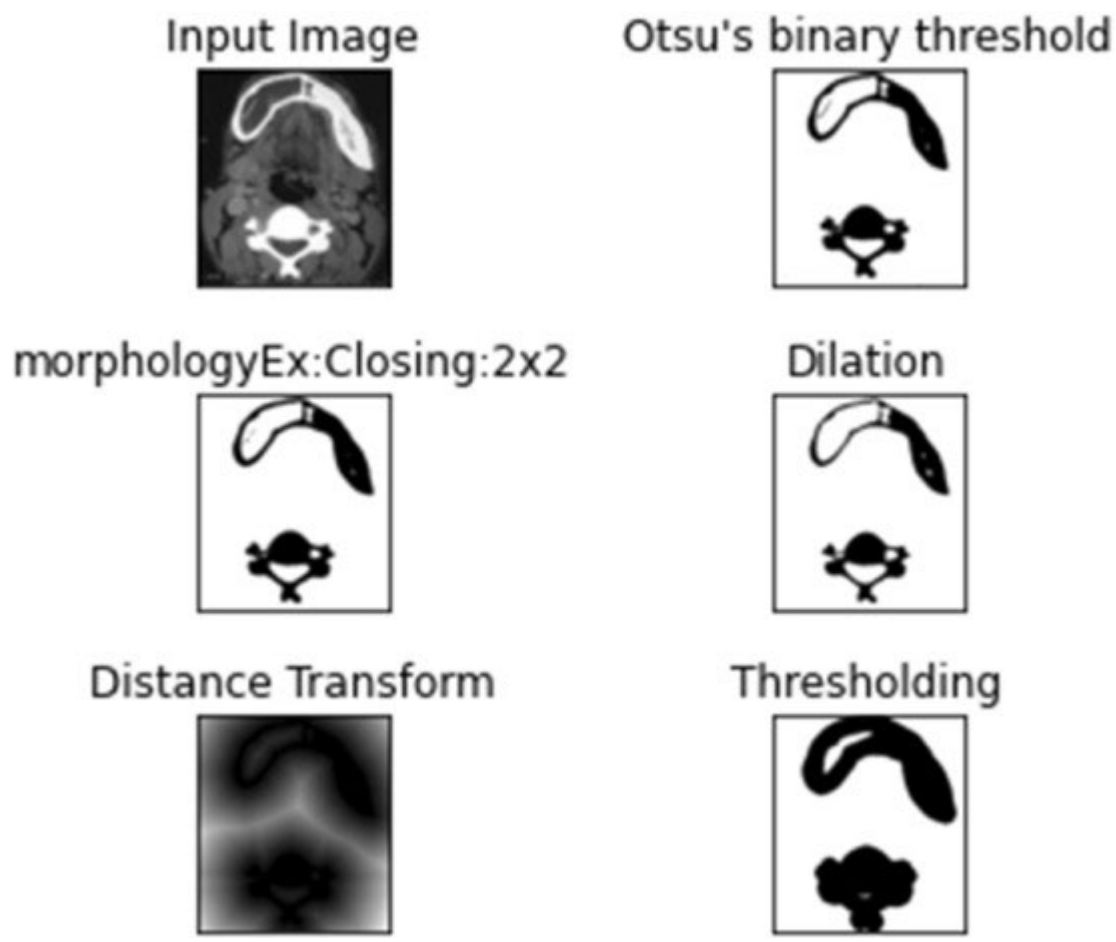


Fig. 8

Watershed region-based image segmentation

Clustering-based image segmentation is grouping similar pixel intensity for analyzing the hidden details of an image. Increasing the number of cluster centers improves the segmentation accuracy by grouping the shades, texture, and structures. Clustering techniques of K-means and fuzzy c-means algorithms are used for segmenting the images.

K-means clustering initiates the cluster-based segmentation; then improved clustering is proposed by Akhtar et al. (2014),

$$f = \sum_{j=1}^k \sum_{i=1}^n x_{ij} \cdot y_{ij} - c_j^2$$

where f is the objective function, k is several clusters, c is the clusters' centroids, and n denotes the count of the objects.

Fuzzy clustering is allowing the pixels to group more than one cluster with varying associativity levels (Li and Li 2009). Deep learning principles are applied in different scientific applications (Krishnamoorthy 2021; Bharti et al. 2021). Figure 9 shows the cluster-based segmentation with the number of cluster variations.

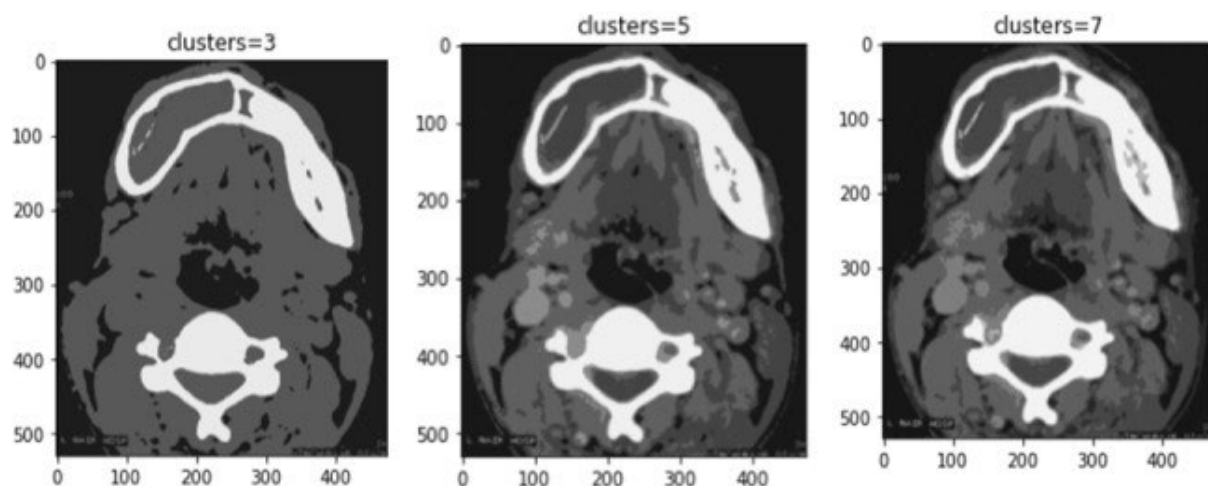


Fig. 9

Cluster-based segmentation

All the fibrous region pixels are segmented and classified into single groups with semantic segmentation algorithms. To differentiate the regions with high- and low-level fibrous formation is identified with different instance segmentation algorithms. Pixels are the real entity to create the meaningful difference from the sharp corners. It defines the object edges and shapes with threshold values. The boundary of the discovered fibrous regions may be discontinuous, and it is covered with local element-wise multiplication.

Transfer learning of tumor detection algorithm is applied into fibrous dysplasia affected image with different iteration and parameter tuning. Mask-RCNN segmentation algorithm is implemented to extract the affected portion of an image. The learning parameters are initiated with default values and user-specific values based on the model architecture. Since the deep learning models need more data samples for training and testing. When the input samples are increased, and the model prediction accuracy is also increased. Cross entropy loss is measured in classifying the fibrous region from the normal bone tissues. This model deals with binary classification.

$\text{CrossEntropyLoss} = -y \log p + 1 - y \log 1 - p$

The filtering approach clears the noisy information from the images. Additionally, clustering approach groups, the similar texture details with their predefined labels. It creates the mask over the fibrous regions with the help of multiple cluster seeds.

Image augmentation is used for increasing the data samples with variations for efficient training. With these augmented images, the exact portion of a tumor or lesion is detected. Figure 10 shows the image segmentation with different parameter tuning in model training with one or more masks.

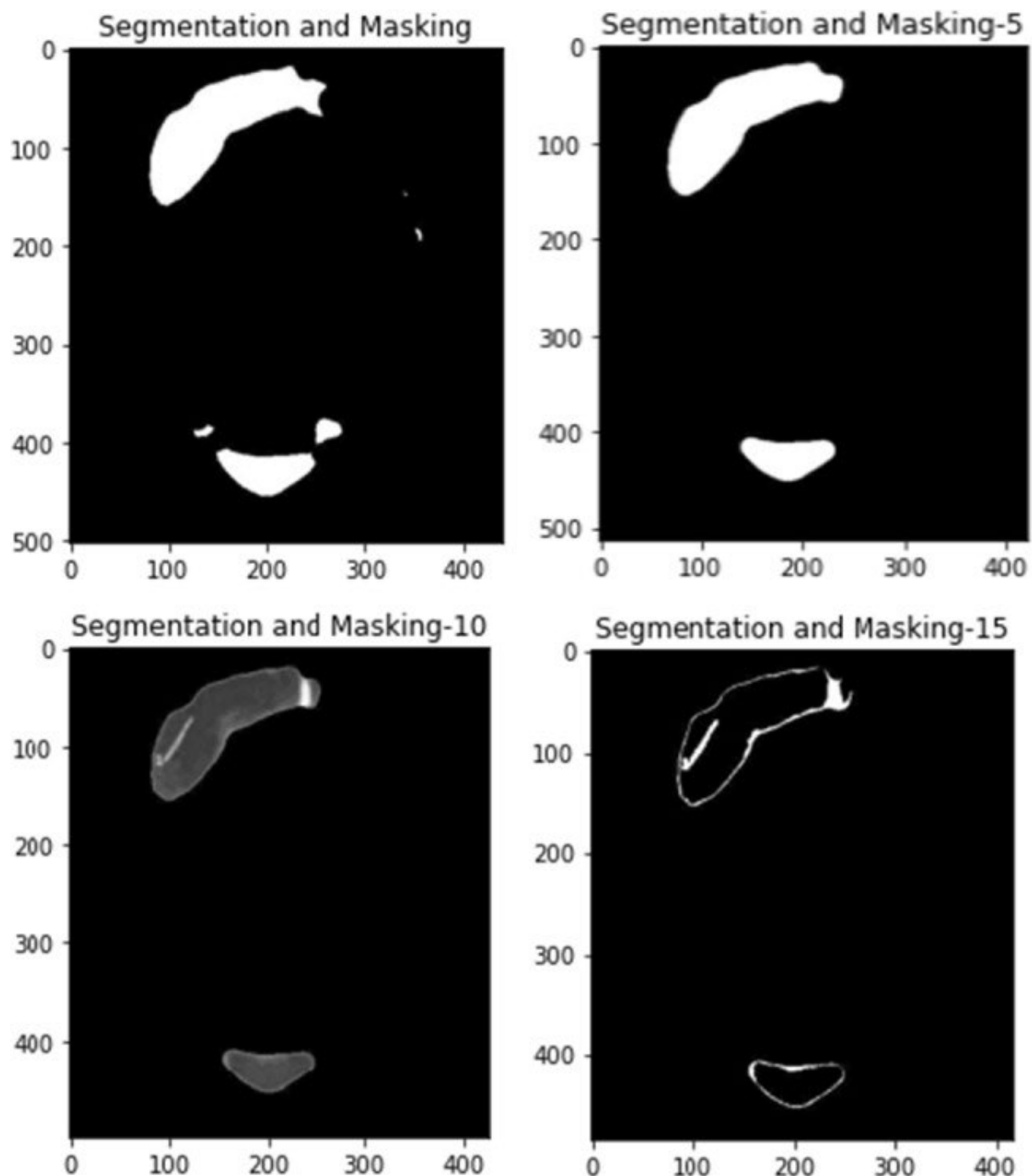


Fig. 10

Transfer learning of tumor detection on FD affected images

The input image contrast pixels are compared with convolutional local features to separate the abnormal regions. Some of the concave portions of the bone images have noisy pixels. This messiness creates the pixel correlation with background information on deciding the edges. The loss values of defining edges are measured and plotted. Figure 11 shows training and testing samples of skull dysplasia segmentation loss.



Fig. 11

Skull dysplasia image segmentation

Discovering the relevant portion segmentation is measured with true detections from all fibrous portion detection.

Precision=TrueDetectionAll_detections

All relevant fields are extracted and form the mapping with ground-truth detected portions.

Recall=TrueDetectionAllground_truths

The hyperparameters of RCNN are succeeded in all 40 iterations. Every step the bounding box construction with the extracted region is estimated perfectly. The average deviation of boundary box loss segmented location is illustrated in Fig. 12.

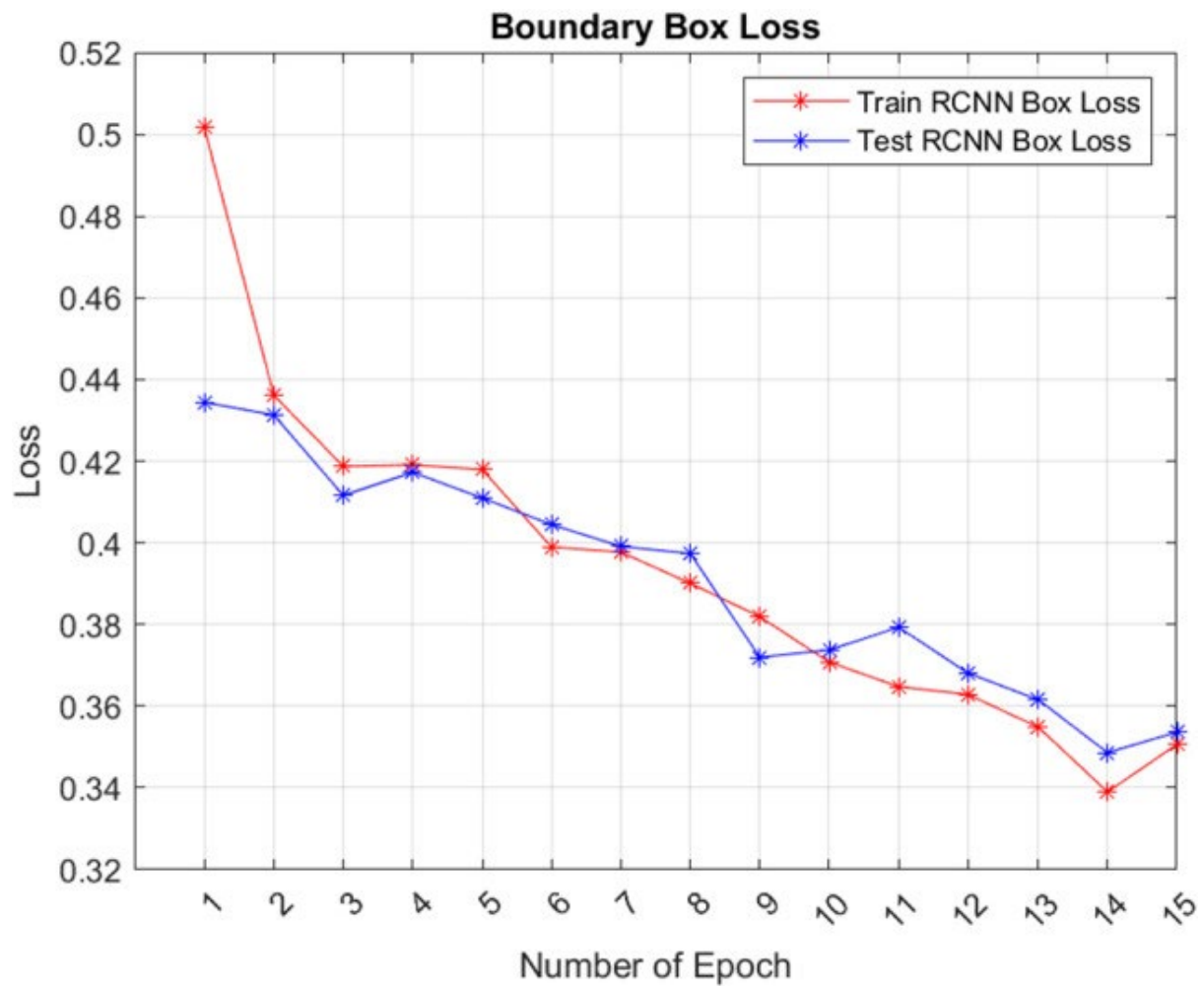


Fig. 12

Building box construction on the segmented region

Figure 13 shows the mask with filled colors of segmented objects based on the edges detected by the algorithm. Highlighting fibrous tissue region from bone marrows is not correctly differentiated. The edge pixel values are assorted with the background information. RCNN works the encoder and decoder model to specify the interconnected pixels in the receptive field. These high-density interconnected pixels define the region over the field.

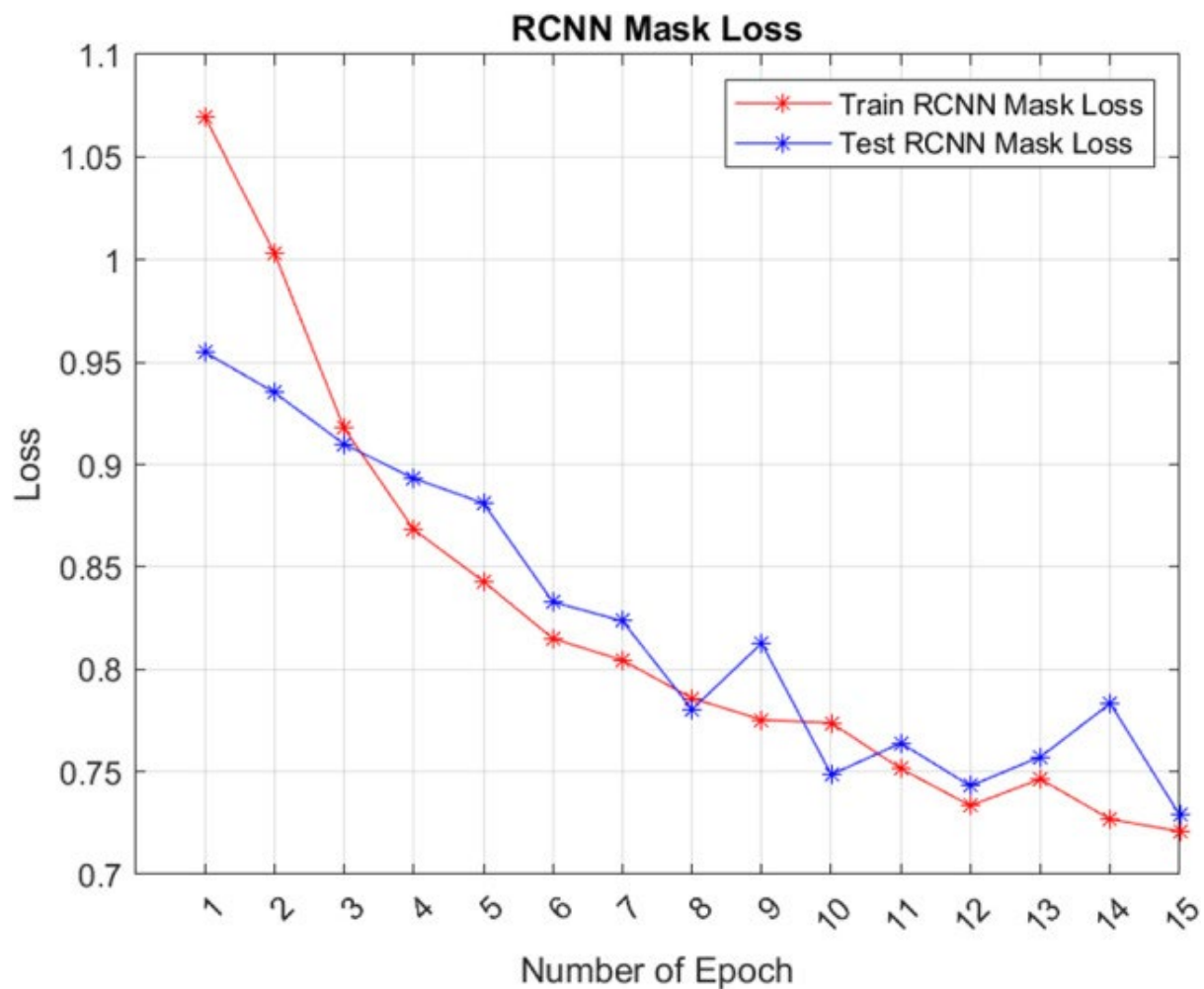


Fig. 13

Mask on the segmented region

Conclusion

Different prospects of medical image error analysis techniques are discussed with fibrous dysplasia-affected samples. Bone density and bone thickness techniques are discussed with quantitative measures of the bone test. Various pre-processing techniques of classical and learning-based filters are applied in the FD images. It extracts the essential features of texture, brightness, smoothing, shades, intensities, structures, and edges of the images. Irrelevant information is reduced with filtering techniques by sharpening the edges. The Pre-processed image is forwarded to image segmentation for fibrous tissue detection and localization. Six different types of segmentation algorithms are applied in the FD affected sample, to identify the bulges, lesions, dis-alignment of bone structures and fibrous tissue growth inside the bone. Further improvements of this work are to enhance the convolutional neural network for classifying several FD abnormalities with multi-class abnormality prediction and also need to focus on illuminance noise removal algorithms.

Acknowledgements

This work was supported by the Researchers Supporting Project (No. RSP-2021/395), King Saud University, Riyadh, Saudi Arabia.

Author contributions

The first author contributed to concept and investigation techniques. The second author contributed to supervision and guidance. The third author involved in providing the resources, and the fourth author involved in reviews and editing.

Data availability

The data and findings are incorporated with another progressive work. These results are not shared publicly by this time because of the ongoing research work.

Declarations

Conflict of interest

The authors declare no conflict of interest.

Ethical approval

This article does not contain any studies with human participants or animal performed by any of the authors.

Footnotes

Publisher's Note

Springer Nature remains neutral with regard to jurisdictional claims in published maps and institutional affiliations.

Contributor Information

A. Saranya, Email: moc.liamg@21timaynaras.

Kottilingam Kottursamy, Email: ni.ude.tsimrs@kilittok.

Ahmad Ali AlZubi, Email: as.ude.usk@ibuzlaa.

Ali Kashif Bashir, Email: gro.eeei@b.fihsakila.rd.

References

1. Ahmad M, Bashir AK, Khan AM. Metric similarity regularizer to enhance pixel similarity performance for hyperspectral unmixing. *Optik*. 2017;140:86–95. doi: 10.1016/j.ijleo.2017.03.051. [[CrossRef](#)] [[Google Scholar](#)]
2. Akhtar N, Agarwal N, Burjwal A (2014) K-mean algorithm for image segmentation using neutrosophy. In: 2014 international conference on advances in computing, communications and informatics (ICACCI), IEEE, pp 2417–2421
3. Alabdulatif A, Khalil I, Yi X, Guizani M. Secure edge of things for smart healthcare surveillance framework. *IEEE Access*. 2019;7:31010–31021. doi: 10.1109/ACCESS.2019.2899323. [[CrossRef](#)] [[Google Scholar](#)]
4. Alkouz B, Al Aghbari Z, Abawajy JH. Tweetluenza: predicting flu trends from twitter data. *Big Data Min. Anal*. 2019;2(4):273–287. doi: 10.26599/BDMA.2019.9020012. [[CrossRef](#)] [[Google Scholar](#)]

5. Ang IC, Fox M, Polk JD, Kersh ME. An algorithm for automated separation of trabecular bone from variably thick cortices in high-resolution computed tomography data. *IEEE Trans Biomed Eng.* 2019;67(3):924–930. doi: 10.1109/TBME.2019.2924398. [[Abstract](#)] [[CrossRef](#)] [[Google Scholar](#)]
6. Areeckal AS, Sam M, David SS (2018) Computerized radiogrammetry of third metacarpal using watershed and active appearance model. In: 2018 IEEE international conference on industrial technology (ICIT), IEEE, 2018, pp 1490–1495
7. Areeckal AS, Kocher M. Current and emerging diagnostic imaging-based techniques for assessment of osteoporosis and fracture risk. *IEEE Rev Biomed Eng.* 2018;12:254–268. doi: 10.1109/RBME.2018.2852620. [[Abstract](#)] [[CrossRef](#)] [[Google Scholar](#)]
8. Bachrach LK, Hastie T, Wang M-C, Narasimhan B, Marcus R. Bone mineral acquisition in healthy Asian, Hispanic, black, and Caucasian youth: a longitudinal study. *J Clin Endocrinol Metab.* 1999;84(12):4702–4712. [[Abstract](#)] [[Google Scholar](#)]
9. Bharti JP, Mishra P, Sathishkumar VE, Cho Y, Samui P (2021) Slope stability analysis using Rf, Gbm, Cart, Bt and Xgboost. *Geotech Geol Eng*, 39(5): 3741–3752
10. Brosch T, Tang LY, Yoo Y, Li DK, Traboulsee A, Tam R. Deep 3D convolutional encoder networks with shortcuts for multiscale feature integration applied to multiple sclerosis lesion segmentation. *IEEE Trans Med Imaging.* 2016;35(5):1229–1239. doi: 10.1109/TMI.2016.2528821. [[Abstract](#)] [[CrossRef](#)] [[Google Scholar](#)]
11. Buckeridge DL, Izadi M, Shaban-Nejad A, Mondor L, Jauvin C, Dube L, Tamblyn R. An infrastructure for real-time population health assessment and monitoring. *IBM J Res Dev.* 2012;56(5):2–1. doi: 10.1147/JRD.2012.2197132. [[CrossRef](#)] [[Google Scholar](#)]
12. Byeon W, Breuel TM, Raue F, Liwicki M (2015) Scene labeling with lstm recurrent neural networks. In: *Proceedings of the IEEE conference on computer vision and pattern recognition*, pp 3547–3555
13. Cabral HWS, Andolphi BFG, Ferreira BVC, Alves DCF, Morelato RL, Chambo A, Borges LS. The use of biomarkers in clinical osteoporosis. *Revista da Associação Médica Brasileira.* 2016;62:368–376. doi: 10.1590/1806-9282.62.04.368. [[Abstract](#)] [[CrossRef](#)] [[Google Scholar](#)]
14. Chen L-C, Papandreou G, Kokkinos I, Murphy K, Yuille AL. Deeplab: Semantic image segmentation with deep convolutional nets, atrous convolution, and fully connected crfs. *IEEE Trans Pattern Anal Mach Intell.* 2017;40(4):834–848. doi: 10.1109/TPAMI.2017.2699184. [[Abstract](#)] [[CrossRef](#)] [[Google Scholar](#)]
15. Chen Bo, Qiu hao Xu, Wang L, Leung S, Chung J, Li S. An automated and accurate spine curve analysis system. *IEEE Access.* 2019;7:124596–124605. doi: 10.1109/ACCESS.2019.2938402. [[CrossRef](#)] [[Google Scholar](#)]
16. Cireşan DC, Giusti A, Gambardella LM, Schmidhuber J (2013) Mitosis detection in breast cancer histology images with deep neural networks. In: *International conference on medical image computing and computer-assisted intervention*, Springer, Berlin, pp 411–418 [[Abstract](#)]

17. de Jong JJ, Heyer FL, Arts JJ, Poeze M, Keszei AP, Willems PC, van den Bergh JP. Fracture repair in the distal radius in postmenopausal women: a follow-up 2 years Postfracture using HRpQCT. *J Bone Min Res.* 2016;31(5):1114–1122. doi: 10.1002/jbmr.2766. [[Abstract](#)] [[CrossRef](#)] [[Google Scholar](#)]
18. Diez-Perez A, Gonzalez-Macias J, Marin F, Abizanda M, Alvarez R, Gimeno A, Pegenaute E, Vila J. Prediction of absolute risk of non-spinal fractures using clinical risk factors and heel quantitative ultrasound. *Osteoporos Int.* 2007;18(5):629–639. doi: 10.1007/s00198-006-0297-5. [[Abstract](#)] [[CrossRef](#)] [[Google Scholar](#)]
19. Duan J, Bello G, Schlemper J, Bai W, Dawes TJ, Biffi C, Rueckert D. Automatic 3D bi-ventricular segmentation of cardiac images by a shape-refined multi-task deep learning approach. *IEEE Trans Med Imaging.* 2019;38(9):2151–2164. doi: 10.1109/TMI.2019.2894322. [[Europe PMC free article](#)] [[Abstract](#)] [[CrossRef](#)] [[Google Scholar](#)]
20. Fang Y, Chen Z, Lin W, Lin C-W. Saliency detection in the compressed domain for adaptive image retargeting. *IEEE Trans Image Process.* 2012;21(9):3888–3901. doi: 10.1109/TIP.2012.2199126. [[Abstract](#)] [[CrossRef](#)] [[Google Scholar](#)]
21. Fang Y, Wang J, Narwaria M, Le Callet P, Lin W. Saliency detection for stereoscopic images. *IEEE Trans Image Process.* 2014;23(6):2625–2636. doi: 10.1109/TIP.2014.2305100. [[Abstract](#)] [[CrossRef](#)] [[Google Scholar](#)]
22. Farag A, Le Lu, Roth HR, Liu J, Turkbey E, Summers RM. A bottom-up approach for pancreas segmentation using cascaded superpixels and (deep) image patch labeling. *IEEE Trans Image Process.* 2016;26(1):386–399. doi: 10.1109/TIP.2016.2624198. [[Abstract](#)] [[CrossRef](#)] [[Google Scholar](#)]
23. Fibrous dysplasia | Genetic and Rare Diseases Information Center (GARD) – an NCATS Program (nih.gov).
24. Fourati WA, Bouhlef MS. Trabecular bone image segmentation using iterative watershed and multi resolution analysis. *Int J Bio-Sci Bio-Technol.* 2011;3(2):71–82. [[Google Scholar](#)]
25. Ghosh S, Raja'S A, Chaudhary V, Dhillon G (2011) Automatic lumbar vertebra segmentation from clinical CT for wedge compression fracture diagnosis. In: *Medical imaging 2011: computer-aided diagnosis*, 7963, p. 796303
26. Giordano D, Spampinato C, Scarciofalo G, Leonardi R. An automatic system for skeletal bone age measurement by robust processing of carpal and epiphysal/metaphysal bones. *IEEE Trans Instrum Meas.* 2010;59(10):2539–2553. doi: 10.1109/TIM.2010.2058210. [[CrossRef](#)] [[Google Scholar](#)]
27. Gonzalez RC, Richard EW (2002) *Digital image processing*
28. Guarnieri G, Marsi S, Ramponi G. High dynamic range image display with halo and clipping prevention. *IEEE Trans Image Process.* 2010;20(5):1351–1362. doi: 10.1109/TIP.2010.2092436. [[Abstract](#)] [[CrossRef](#)] [[Google Scholar](#)]
29. Hans D, Krieg M-A. The clinical use of quantitative ultrasound (QUS) in the detection and management of osteoporosis. *IEEE Trans Ultrason Ferroelectr Freq Control.* 2008;55(7):1529–1538. doi: 10.1109/TUFFC.2008.829. [[Abstract](#)] [[CrossRef](#)] [[Google Scholar](#)]

30. Hans D, Hartl F, Krieg MA. Device-specific weighted T-score for two quantitative ultrasounds: operational propositions for the management of osteoporosis for 65 years and older women in Switzerland. *Osteoporos Int*. 2003;14(3):251–258. doi: 10.1007/s00198-002-1358-z. [[Abstract](#)] [[CrossRef](#)] [[Google Scholar](#)]
31. Hassan H, Bashir AK, Abbasi R, Ahmad W, Luo B. Single image defocus estimation by modified gaussian function. *Trans Emerg Telecommun Technol*. 2019;30(6):e361. [[Google Scholar](#)]
32. Hassan H, Bashir AK, Ahmad M, Menon VG, Afridi IU, Nawaz R, Luo B. Real-time image dehazing by superpixels segmentation and guidance filter. *J Real-Time Image Process*. 2021;18(5):1555–1575. doi: 10.1007/s11554-020-00953-4. [[CrossRef](#)] [[Google Scholar](#)]
33. He K, Gkioxari G, Dollár P, Girshick R (2017) Mask r-cnn. In: *Proceedings of the IEEE international conference on computer vision*, pp 2961–2969
34. Huang H, Meng F, Zhou S, Jiang F, Manogaran G. Brain image segmentation based on FCM clustering algorithm and rough set. *IEEE Access*. 2019;7:12386–12396. doi: 10.1109/ACCESS.2019.2893063. [[CrossRef](#)] [[Google Scholar](#)]
35. Kennedy JA, Israel O, Frenkel A, Bar-Shalom R, Azhari H. Super-resolution in PET imaging. *IEEE Trans Med Imaging*. 2006;25(2):137–147. doi: 10.1109/TMI.2005.861705. [[Abstract](#)] [[CrossRef](#)] [[Google Scholar](#)]
36. Korfiatis, Vasileios Ch, Simone Tassani, and George K. Matsopoulos. "A new Ensemble Classification System for fracture zone prediction using imbalanced micro-CT bone morphometrical data." *IEEE journal of biomedical and health informatics* 22, no. 4 2017: 1189–1196. [[Abstract](#)]
37. Koutkias VG, Chouvarda I, Maglaveras N. A multiagent system enhancing home-care health services for chronic disease management. *IEEE Trans Inf Technol Biomed*. 2005;9(4):528–537. doi: 10.1109/TITB.2005.847511. [[Abstract](#)] [[CrossRef](#)] [[Google Scholar](#)]
38. Krishnamoorthy N, Prasad LN, Kumar CP, Subedi B, Abraha HB, Sathishkumar VE (2021) Rice leaf diseases prediction using deep neural networks with transfer learning. *Environ Res*, 198: 111275 [[Abstract](#)]
39. Kumar A, Kim J, Lyndon D, Fulham M, Feng D. An ensemble of fine-tuned convolutional neural networks for medical image classification. *IEEE J Biomed Health Inform*. 2016;21(1):31–40. doi: 10.1109/JBHI.2016.2635663. [[Abstract](#)] [[CrossRef](#)] [[Google Scholar](#)]
40. Kwok SH, Constantinides AG. A fast recursive shortest spanning tree for image segmentation and edge detection. *IEEE Trans Image Process*. 1997;6(2):328–332. doi: 10.1109/83.551705. [[Abstract](#)] [[CrossRef](#)] [[Google Scholar](#)]
41. Kwon SB, Han HS, Lee MC, Kim HC, Ku Y. Machine learning-based automatic classification of knee osteoarthritis severity using gait data and radiographic images. *IEEE Access*. 2020;8:120597–120603. doi: 10.1109/ACCESS.2020.3006335. [[CrossRef](#)] [[Google Scholar](#)]

42. LeCun Y, Bengio Y, Hinton G. Deep learning. *Nature*. 2015;521(7553):436. doi: 10.1038/nature14539. [[Abstract](#)] [[CrossRef](#)] [[Google Scholar](#)]
43. Lee CY, Saining X, Patrick G, Zhengyou Z, Zhuowen T (2015) Deeply-supervised nets. In: *Artificial intelligence and statistics*, PMLR, pp 562–570
44. Li Y, Li G (2009) Fuzzy C-means cluster segmentation algorithm based on modified membership. In: *International symposium on neural networks*, Springer, Berlin, 2009, pp 135–144
45. Li H, Yu K, Liu B, Feng C, Qin Z, Srivastava G. An efficient ciphertext-policy weighted attribute-based encryption for the internet of health things. *IEEE J Biomed Health Inform*. 2021 doi: 10.1109/JBHI.2021.3075995. [[Abstract](#)] [[CrossRef](#)] [[Google Scholar](#)]
46. Lin H-H, Peng S-L, Jay Wu, Shih T-Y, Chuang K-S, Shih C-T. A novel two-compartment model for calculating bone volume fractions and bone mineral densities from computed tomography images. *IEEE Trans Med Imaging*. 2016;36(5):1094–1105. doi: 10.1109/TMI.2016.2646698. [[Abstract](#)] [[CrossRef](#)] [[Google Scholar](#)]
47. Lin TY, Dollár P, Girshick R, He K, Hariharan B, Belongie S (2017) Feature pyramid networks for object detection. In: *Proceedings of the IEEE conference on computer vision and pattern recognition*, pp 2117–2125
48. Liu Y, Jin D, Li C, Janz KF, Burns TL, Torner JC, Levy SM, Saha PK. A robust algorithm for thickness computation at low resolution and its application to in vivo trabecular bone CT imaging. *IEEE Trans Biomed Eng*. 2014;61(7):2057–2069. doi: 10.1109/TBME.2014.2313564. [[Europe PMC free article](#)] [[Abstract](#)] [[CrossRef](#)] [[Google Scholar](#)]
49. Long J, Evan S, Trevor D (2015) Fully convolutional networks for semantic segmentation. In: *Proceedings of the IEEE conference on computer vision and pattern recognition*, pp 3431–3440
50. Looker AC, Bauer DC, Chesnut Iii CH, Gundberg CM, Hochberg MC, Klee G, Bell NH. Clinical use of biochemical markers of bone remodeling: current status and future directions. *Osteoporosis Int*. 2000;11(6):467–480. doi: 10.1007/s001980070088. [[Abstract](#)] [[CrossRef](#)] [[Google Scholar](#)]
51. Mallick PK, Ryu SH, Satapathy SK, Mishra S, Nguyen GN, Tiwari P. Brain MRI image classification for cancer detection using deep wavelet autoencoder-based deep neural network. *IEEE Access*. 2019;7:46278–46287. doi: 10.1109/ACCESS.2019.2902252. [[CrossRef](#)] [[Google Scholar](#)]
52. Manzke R, Meyer C, Ecabert O, Peters J, Noordhoek NJ, Thiagalingam A, Reddy VY, Chan RC, Weese J. Automatic segmentation of rotational X-ray images for anatomic intra-procedural surface generation in atrial fibrillation ablation procedures. *IEEE Trans Med Imaging*. 2009;29(2):260–272. doi: 10.1109/TMI.2009.2021946. [[Abstract](#)] [[CrossRef](#)] [[Google Scholar](#)]
53. Mazess R, Collick B, Trempe J, Barden H, Hanson J. Performance evaluation of a dual-energy X-ray bone densitometer. *Calcif Tissue Int*. 1989;44(3):228–232. doi: 10.1007/BF02556569. [[Abstract](#)] [[CrossRef](#)] [[Google Scholar](#)]

54. Mehra R, Pachpor K, Kottilingam K, Saranya A (2020) An initiative to prevent japanese encephalitis using genetic algorithm and artificial neural network. In: 2020 international conference on computational intelligence (ICCI), pp 142–148. IEEE
55. Meyer F. Topographic distance and watershed lines. *Signal Process.* 1994;38(1):113–125. doi: 10.1016/0165-1684(94)90060-4. [[CrossRef](#)] [[Google Scholar](#)]
56. Milletari F, Navab N, Ahmadi SA (2016) V-net: fully convolutional neural networks for volumetric medical image segmentation. In: 2016 fourth international conference on 3D vision (3DV), pp 565–571. IEEE
57. Minaee S, Boykov YY, Porikli F, Plaza AJ, Kehtarnavaz N, Terzopoulos D (2021) Image segmentation using deep learning: a survey. *IEEE Trans Pattern Anal Mach Intell.* [[Abstract](#)]
58. Nazarian A, von Stechow D, Zurakowski D, Müller R, Snyder BD. Bone volume fraction explains the variation in strength and stiffness of cancellous bone affected by metastatic cancer and osteoporosis. *Calcified Tissue Int.* 2008;83(6):368–379. doi: 10.1007/s00223-008-9174-x. [[Abstract](#)] [[CrossRef](#)] [[Google Scholar](#)]
59. Nguyen N-Q, Lee S-W. Robust boundary segmentation in medical images using a consecutive deep encoder-decoder network. *Ieee Access.* 2019;7:33795–33808. doi: 10.1109/ACCESS.2019.2904094. [[CrossRef](#)] [[Google Scholar](#)]
60. Njeh CF, Hans D, Li J, Fan B, Fuerst T, He YQ, Tsuda-Futami E, Lu Y, Wu CY, Genant HK. Comparison of six calcaneal quantitative ultrasound devices: precision and hip fracture discrimination. *Osteoporos Int.* 2000;11(12):1051–1062. doi: 10.1007/s001980070027. [[Abstract](#)] [[CrossRef](#)] [[Google Scholar](#)]
61. O'Reilly MA, Hynynen K. A super-resolution ultrasound method for brain vascular mapping. *Medical Phys.* 2013;40(11):110701. doi: 10.1118/1.4823762. [[Europe PMC free article](#)] [[Abstract](#)] [[CrossRef](#)] [[Google Scholar](#)]
62. Ohlsson C, Sundh D, Wallerik A, Nilsson M, Karlsson M, Johansson H, Mellström D, Lorentzon M. Cortical bone area predicts incident fractures independently of areal bone mineral density in older men. *J Clin Endocrinol Metab.* 2017;102(2):516–524. [[Abstract](#)] [[Google Scholar](#)]
63. Oksuz I, Ruijsink B, Puyol-Antón E, Clough JR, Cruz G, Bustin A, Prieto C, Botnar R, Rueckert D, Schnabel JA, King AP. Automatic CNN-based detection of cardiac MR motion artefacts using k-space data augmentation and curriculum learning. *Med Image Anal.* 2019;55:136–147. doi: 10.1016/j.media.2019.04.009. [[Europe PMC free article](#)] [[Abstract](#)] [[CrossRef](#)] [[Google Scholar](#)]
64. Oktay O, Ferrante E, Kamnitsas K, Heinrich M, Bai W, Caballero J, Rueckert D. Anatomically constrained neural networks (ACNNs): application to cardiac image enhancement and segmentation. *IEEE Trans Med Imaging.* 2017;37(2):384–395. doi: 10.1109/TMI.2017.2743464. [[Abstract](#)] [[CrossRef](#)] [[Google Scholar](#)]
65. Ram S, Zhang W, Williams M, Pengetnze Y. Predicting asthma-related emergency department visits using big data. *IEEE J Biomed Health Inform.* 2015;19(4):1216–1223. doi: 10.1109/JBHI.2015.2404829. [[Abstract](#)] [[CrossRef](#)] [[Google Scholar](#)]

66. Rao VSH, Kumar MN. A new intelligence-based approach for computer-aided diagnosis of dengue fever. *IEEE Trans Inf Technol Biomed.* 2011;16(1):112–118. doi: 10.1109/TITB.2011.2171978. [[Abstract](#)] [[CrossRef](#)] [[Google Scholar](#)]
67. Ren X, Li T, Yang X, Wang S, Ahmad S, Xiang L, Wang Q. Regression convolutional neural network for automated pediatric bone age assessment from hand radiograph. *IEEE J Biomed Health Inform.* 2018;23(5):2030–2038. doi: 10.1109/JBHI.2018.2876916. [[Abstract](#)] [[CrossRef](#)] [[Google Scholar](#)]
68. Ren S, He K, Girshick R, Sun J (2015) Faster r-cnn: towards real-time object detection with region proposal networks. *arXiv preprint <https://arxiv.org/abs/1506.01497>* 2015 [[Abstract](#)]
69. Ribeiro SS. Using SimpleCV for seed metadata extraction into XML document. *Iberoamerican J Appl Comput.* 2014;4:29. [[Google Scholar](#)]
70. Ronneberger O, Fischer P, Brox T (2015) U-net: convolutional networks for biomedical image segmentation. In: *International conference on medical image computing and computer-assisted intervention*, pp 234–241. Springer, Cham
71. Saha PK, Yan Xu, Duan H, Heiner A, Liang G. Volumetric topological analysis: a novel approach for trabecular bone classification on the continuum between plates and rods. *IEEE Trans Med Imaging.* 2010;29(11):1821–1838. doi: 10.1109/TMI.2010.2050779. [[Europe PMC free article](#)] [[Abstract](#)] [[CrossRef](#)] [[Google Scholar](#)]
72. Saif AFM, Shahnaz C, Zhu WP, Ahmad MO. Abnormality detection in musculoskeletal radiographs using capsule network. *IEEE Access.* 2019;7:81494–81503. doi: 10.1109/ACCESS.2019.2923008. [[CrossRef](#)] [[Google Scholar](#)]
73. Santhoshini P, Tamilselvi R, Sivakumar R. Automatic segmentation of femur bone features and analysis of osteoporosis. *Lect Notes Softw Eng.* 2013;1(2):194. doi: 10.7763/LNSE.2013.V1.44. [[CrossRef](#)] [[Google Scholar](#)]
74. Seyedhosseini M, Tasdizen T. Semantic image segmentation with contextual hierarchical models. *IEEE Trans Pattern Anal Mach Intell.* 2015;38(5):951–964. doi: 10.1109/TPAMI.2015.2473846. [[Europe PMC free article](#)] [[Abstract](#)] [[CrossRef](#)] [[Google Scholar](#)]
75. Su H, Xing F, Kong X, Xie Y, Zhang S, Yang L (2015) Robust cell detection and segmentation in histopathological images using sparse reconstruction and stacked denoising autoencoders. In: *International conference on medical image computing and computer-assisted intervention*, Springer, Cham, pp 383–390 [[Europe PMC free article](#)] [[Abstract](#)]
76. Sun L, Shao W, Zhang D, Liu M. Anatomical attention guided deep networks for ROI segmentation of brain MR images. *IEEE Trans Med Imaging.* 2019;39(6):2000–2012. doi: 10.1109/TMI.2019.2962792. [[Abstract](#)] [[CrossRef](#)] [[Google Scholar](#)]
77. Sun Y, Liu J, Yu K, Alazab M, Lin K. PMRSS: privacy-preserving medical record searching scheme for intelligent diagnosis in IoT healthcare. *IEEE Trans Ind Inform.* 2021 doi: 10.1109/TII.2021.3070544. [[CrossRef](#)] [[Google Scholar](#)]
78. Tan L, Yu K, Shi N, Yang C, Wei W, Lu H. towards secure and privacy-preserving data sharing for COVID-19 medical records: a blockchain-empowered approach. *IEEE Trans Netw Sci Eng.* 2021 doi: 10.1109/TNSE.2021.3101842. [[CrossRef](#)] [[Google Scholar](#)]

79. VanReeth E, Tham IW, Tan CH, Poh CL. Super-resolution in magnetic resonance imaging: a review. *Concepts Magn Resonance Part A*. 2012;40(6):306–325. doi: 10.1002/cmr.a.21249. [[CrossRef](#)] [[Google Scholar](#)]
80. Vedaiei SS, Fotovvat A, Mohebbian MR, Rahman GM, Wahid KA, Babyn P, Sami R. COVID-SAFE: an IoT-based system for automated health monitoring and surveillance in post-pandemic life. *IEEE Access*. 2020;8:188538–188551. doi: 10.1109/ACCESS.2020.3030194. [[Europe PMC free article](#)] [[Abstract](#)] [[CrossRef](#)] [[Google Scholar](#)]
81. Wang G, Zuluaga MA, Li W, Pratt R, Patel PA, Aertsen M, Vercauteren T. DeepIGeoS: a deep interactive geodesic framework for medical image segmentation. *IEEE Trans Pattern Anal Mach Intell*. 2018;41(7):1559–1572. doi: 10.1109/TPAMI.2018.2840695. [[Europe PMC free article](#)] [[Abstract](#)] [[CrossRef](#)] [[Google Scholar](#)]
82. Wang Yi, Dou H, Xiaowei Hu, Zhu L, Yang X, Ming Xu, Qin J, Heng P-A, Wang T, Ni D. Deep attentive features for prostate segmentation in 3D transrectal ultrasound. *IEEE Trans Med Imaging*. 2019;38(12):2768–2778. doi: 10.1109/TMI.2019.2913184. [[Abstract](#)] [[CrossRef](#)] [[Google Scholar](#)]
83. Wehrli FW, Gomberg BR, Saha PK, Song HK, Hwang SN, Snyder PJ. Digital topological analysis of in vivo magnetic resonance microimages of trabecular bone reveals structural implications of osteoporosis. *J Bone Min Res*. 2001;16(8):1520–1531. doi: 10.1359/jbmr.2001.16.8.1520. [[Abstract](#)] [[CrossRef](#)] [[Google Scholar](#)]
84. Xing F, Xie Y, Su H, Liu F, Yang L. Deep learning in microscopy image analysis: a survey. *IEEE Trans Neural Netw Learn Syst*. 2017;29(10):4550–4568. doi: 10.1109/TNNLS.2017.2766168. [[Abstract](#)] [[CrossRef](#)] [[Google Scholar](#)]
85. Yin P, Yuan R, Cheng Y, Wu Q. Deep guidance network for biomedical image segmentation. *IEEE Access*. 2020;8:116106–116116. doi: 10.1109/ACCESS.2020.3002835. [[CrossRef](#)] [[Google Scholar](#)]
86. Yu K, Tan L, Lin L, Cheng X, Yi Z, Sato T. Deep-learning-empowered breast cancer auxiliary diagnosis for 5GB remote E-health. *IEEE Wirel Commun*. 2021;28(3):54–61. doi: 10.1109/MWC.001.2000374. [[CrossRef](#)] [[Google Scholar](#)]
87. Zhang J, Yan CH, Chui CK, Ong SH. Accurate measurement of bone mineral density using clinical CT imaging with single energy beam spectral intensity correction. *IEEE Trans Med Imaging*. 2010;29(7):1382–1389. doi: 10.1109/TMI.2010.2045767. [[Abstract](#)] [[CrossRef](#)] [[Google Scholar](#)]
88. Zhang L, Le Lu, Nogues I, Summers RM, Liu S, Yao J. DeepPap: deep convolutional networks for cervical cell classification. *IEEE J Biomed Health Inform*. 2017;21(6):1633–1643. doi: 10.1109/JBHI.2017.2705583. [[Abstract](#)] [[CrossRef](#)] [[Google Scholar](#)]
89. Zhang Y-Z, Yamaguchi R, Imoto S, Miyano S. Sequence-specific bias correction for RNA-seq data using recurrent neural networks. *BMC Genomics*. 2017;18(1):1–6. doi: 10.1186/s12864-016-3406-7. [[Europe PMC free article](#)] [[Abstract](#)] [[CrossRef](#)] [[Google Scholar](#)]
90. Zhao F, Xie X. An overview of interactive medical image segmentation. *Ann BMVA*. 2013;2013(7):1–22. [[Google Scholar](#)]

91. Zheng S, Jayasumana S, Romera-Paredes B, Vineet V, Su Z, Du D, Torr PH (2015) Conditional random fields as recurrent neural networks. In: Proceedings of the IEEE international conference on computer vision, pp 1529–1537